

# Metastable nitric acid trihydrate in ice clouds

Fabian Weiss, Frank Kubel, Óscar Gálvez,  
Markus Hoelzel, Stewart F. Parker, Philipp  
Baloh, Riccardo Iannarelli, Michel J. Rossi and  
Hinrich Grothe

## Published version information

This is the peer reviewed version of the following article:

**Citation:** Weiss F et al. "Metastable nitric acid trihydrate in ice clouds".  
Angewandte Chemie International Edition, vol. 55, no. 10 (2016): 3276–3280

which has been published in final form at [10.1002/anie.201510841](https://doi.org/10.1002/anie.201510841). This article may be used for non-commercial purposes in accordance With Wiley-VCH Terms and Conditions for self-archiving.

Please cite only the published version using the reference above.

# Metastable Nitric Acid Trihydrate in Ice Clouds

Fabian Weiss, Frank Kubel, Óscar Gálvez, Markus Hoelzel, Stewart F. Parker, Philipp Baloh, Riccardo Iannarelli, Michel J. Rossi and Hinrich Grothe\*

**Abstract:** The composition of high altitude ice clouds is still a matter of intense discussion. The constituents in question are ice and nitric acid hydrates. The identification and formation mechanisms, however, are still unknown but are essential to understand atmospheric processing such as the seasonal ozone depletion in the lower polar stratosphere or the radiation balance of planet Earth. We found conclusive evidence for a long-predicted phase, which has been named alpha nitric acid trihydrate (alpha-NAT). This phase has been characterized by a combination of X-ray and neutron diffraction experiments allowing a convincing structure solution. Additionally, vibrational spectra (infrared and inelastic neutron scattering) were recorded and compared with theoretical calculations. A strong affinity between water ice and alpha-NAT has been found, which explains the experimental spectra and the phase transition kinetics essential for identification in the atmosphere. On the basis of our results, we propose a new three-step mechanism for NAT-formation in high altitude ice clouds.

Nitric acid trihydrate (NAT) is an important constituent of Polar Stratospheric Clouds (PSCs) [1]. Balloon flights [2-3] as well as satellite FTIR measurements accompanied by ground based LIDAR observed NAT in a mixture with ice [4]. Homogeneous nucleation rates of NAT (upper limit  $3 \times 10^{-10} \text{ cm}^{-3} \text{ air h}^{-1}$ ) have been found to be much too low for cloud formation [5-6] therefore heterogeneous nucleation on ice or on micrometeorites has been proposed [7-8]. The large barrier for homogenous nucleation may be the reason why NAT has never been observed in cloud chamber experiments, because of the lack of both the time needed for homogeneous freezing of ice as well as the corresponding nuclei for heterogeneous freezing [9]. In 2004 a research consortium of the National Oceanic and Atmospheric Administration (NOAA) also detected NAT in cirrus clouds and in

contrails [10]. As a consequence, and combined with the fact that the level of water vapour is much too high in these clouds, Gao et al. [11] have set-up a model, which explains, at least theoretically, the conditions in these high altitude ice clouds.

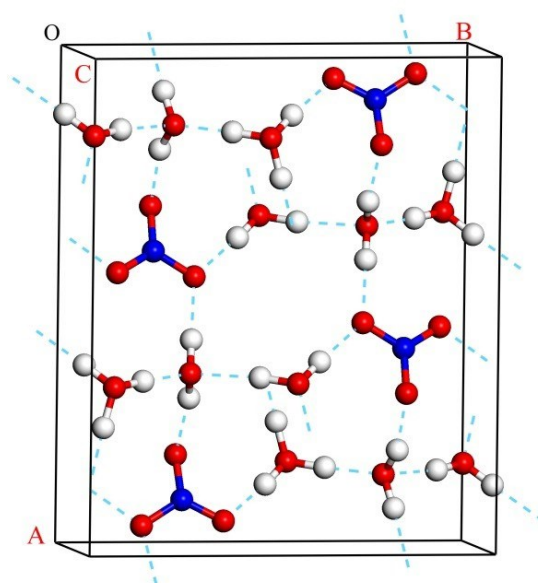


**Figure 1:** Unit cell of the alpha-NAT structure; axes: A, B, C (origin O); spheres: oxygen-red, nitrogen-blue, hydrogen-grey; bonds: solid sticks-covalent bonds, turquoise dots-hydrogen bonds

The idea of Gao et al. [11] was that in the upper troposphere (UT) not the thermodynamically stable and well-known hexagonal ice is formed but rather the so-called Ice of Complex Habit (named Delta Ice). Here, the ice is a mixture of hexagonal ( $P6_3/mmc$ ) and cubic ice ( $Fd\bar{3}m$ ), (although later studies point to stacking faults and symmetry reduction [12-13] being present), and the surface of the solid particles may be covered by NAT. The surface coverage and the metastable phases together suppress further growth of the crystalline particles, which leads to an elevated water vapor pressure and this is exactly what field experiments have found.

We assume that instead of the thermodynamically stable beta-NAT, metastable NAT (alpha-NAT) is formed first, which explains the results obtained in laboratory experiments and observations. Interestingly, alpha-NAT has not been acknowledged by many atmospheric scientists and most papers in the field just focus on beta-NAT, which is thermodynamically stable. However, under the conditions of the lower stratosphere and the upper troposphere alpha-NAT can persist for several hours and when it occurs in a mixture with ice it can even persist for more than a day [14]. Unfortunately, the crystalline structure of alpha-NAT is unknown until now, which has hampered its spectroscopic

[\*] Prof. Dr. H. Grothe, F. Weiss, P. Baloh  
Institut fuer Materialchemie, Technische Universitaet Wien  
Getreidemarkt 9/BC/01, 1060 Wien (Austria)  
Fax: (+43) 1-58801-9-165122  
E-mail: grothe@tuwien.ac.at  
Homepage: <http://www.imc.tuwien.ac.at>  
Prof. Dr. F. Kubel  
Institut fuer Chemische Technologie und Analytik, TU Wien  
Dr. O. Gálvez  
Instituto de Estructura de la Materia, IEM-CSIC, Madrid (Spain)  
Dr. M. Hoelzel  
Forschungsbereich Neutronenquelle Heinz Maier-Leibnitz (FRM II),  
Technische Universität München (Germany)  
Dr. S. F. Parker  
ISIS Facility, STFC Rutherford Appleton Laboratory, Chilton, Didcot,  
OX11 0QX (UK)  
Dr. M. J. Rossi, Dr. R. Iannarelli, Paul-Scherrer Institute, 5232  
Villigen (Switzerland)

identification. Spectroscopic data from the laboratory are, however, essential to identify the composition of ice clouds, which relies solely on remote sensing.

Due to its metastability it was not possible to grow a single crystal of alpha-NAT, but a pure crystalline powder was accessible. It is generally more difficult to deduce a complex crystalline structure from powder diffraction data alone. Nevertheless, we were successful in the present case and have for the first time solved the complete structure of alpha-NAT. When critically comparing the new structure (monoclinic,  $P2_1/a$  – Fig. 1) with the known structure of the beta phase (orthorhombic,  $P2_12_12_1$ ), one may recognize that the alpha structure exhibits a lower symmetry but similar cell volume [15]. However, this structure completely fits both the X-ray and neutron diffraction data, which were independently recorded on samples prepared in the same way (see Fig. 2). The refinement has been performed with the program package TOPAS 4.2 [16] and the conformities are very high (reliability factors  $R_{\text{prof}}$  and  $wR_{\text{prof}}$  are below 5%). This is the first unambiguous proof of the existence of the alpha-NAT phase by diffraction techniques. All former conclusions were only drawn from spectroscopic data.

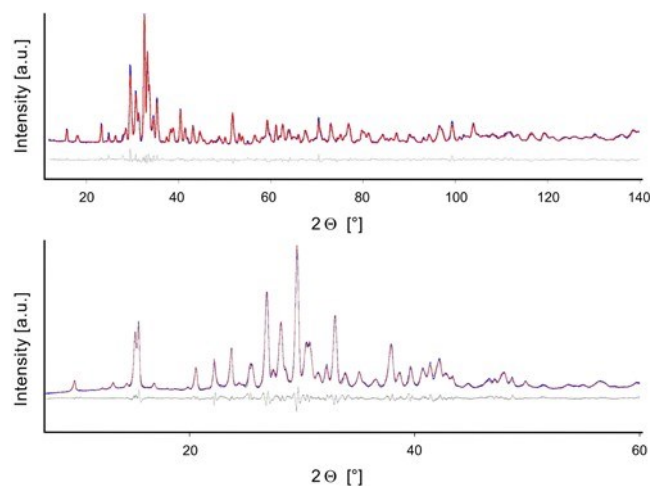


**Figure 2:** Top panel: neutron diffractogram of alpha NAT generated at 159K and measured at 4K; Bottom Panel X-ray diffractogram of alpha NAT generated at 155K; Red: experimental data / Blue: calculated data / Grey: difference

This newly derived structure was used to calculate the infrared (IR) and inelastic neutron scattering (INS) spectra and compared with those experimentally recorded (see Fig. 3). In both spectra, band positions have been found with reasonable accuracy, regarding the limitations of the calculations (the use of the harmonic approximation and no model for calculating the width of the IR bands). For the INS, there is missing intensity at 80 and 520  $\text{cm}^{-1}$ . These bands can be assigned to the acoustic translations and the librational modes in crystalline ice, which are present in all experiments [17]. In the case of the IR spectra (right panel in Fig. 3), as mentioned above the calculations do not provide information about the width of the bands, and those are arbitrarily represented by Lorentzians with a FWHM of 80  $\text{cm}^{-1}$  for all wavenumbers except for the OH stretching bands of  $\text{H}_3\text{O}^+$  (bands around 2900–2700  $\text{cm}^{-1}$ ) for which a larger width of 200  $\text{cm}^{-1}$  has been used based on previous studies [18]. Nevertheless, in spite of these limitations, most band positions of the IR experimental spectrum are appropriately reproduced. However, the very narrow band at 3450  $\text{cm}^{-1}$  which appears in the experimental spectra as a characteristic pattern is not reproduced in the calculations and cannot be attributed to the intrinsic limitations of the theoretical method (see SI section). Therefore,

we deduce that this OH stretching vibration is not related to alpha-NAT but is assigned to small crystalline ice clusters, which exhibit dangling OH bonds.

A possible reason we were never able to prepare alpha-NAT in its pure water-free form (as was mentioned above in the analysis of the vibrational spectra) might be based upon its larger affinity towards water than beta-NAT, due to differences in the structure. To test this hypothesis we deposited  $\text{HNO}_3$  vapor on a pure water ice film at relevant stratospheric temperatures. A deconvolution of the composite IR absorption spectrum reveals that it consists of a mixture of alpha-NAT and pure  $\text{H}_2\text{O}$  ice, but not beta-phase, although on annealing, alpha-NAT finally transforms into beta-NAT [19]. Tables S2a and S2b in the Supplementary Information section list the characteristic peak positions of alpha- and beta-NAT, which were observed in the range of 170–190 K and 183–200 K, respectively, in the present work. The growth conditions have been chosen in order to simulate polar stratospheric conditions as far as temperature is concerned (details are given in the supplement section as well).

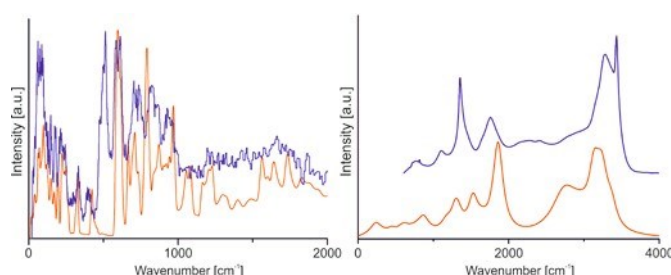


**Figure 3:** Left panel: inelastic neutron scattering alpha-NAT Right panel: IR spectra of alpha-NAT; Blue: experimental data / Red: calculated data as generated from the CASTEP program package.

We emphasize that growth of alpha-NAT occurs without any apparent nucleation barrier under the present conditions once an ice film of sufficient thickness is present. This fact supports the contention made above that the presence of ice stabilizes the metastable alpha-NAT phase. Based on the concise review of Zondlo et al. [20] the present results are at variance in two respects: (i) the formation of a supercooled  $\text{H}_2\text{O}/\text{HNO}_3$  liquid layer before the build-up of a crystalline alpha-NAT phase observed in several studies is not observed under the present conditions; (ii) evaporation of  $\text{H}_2\text{O}$  from the supercooled liquid  $\text{H}_2\text{O}/\text{HNO}_3$  layer was not necessary to form the crystalline alpha-NAT phase. This is in contrast to the majority of past work which has never observed crystallization of NAT at or below the ice frost point of 188 K. Instead, we observe facile formation of the metastable alpha-NAT phase without an apparent nucleation barrier [18]. In earlier kinetic investigations, we have already found such an interaction between ice and alpha-NAT. We could show in kinetic measurements (using XRD) and by cryo-ESEM that alpha-NAT crystals are stabilized when incorporated into an ice matrix and survive up to much higher temperatures than the pure form [14].

With the aim of exploring the interaction between NAT and water, we have carried out quantum chemical calculations on {001} surfaces of alpha- and beta-NAT crystals. More details of these calculations are included in the supporting information. The calculations predict a larger water adsorption energy (5–30 %) for the surface of alpha-NAT compared to beta-NAT, which is in agreement with our hypothesis. Figure 4 shows a representation of the adsorption of a six-membered-ring of water molecules on a {001} surface of alpha-NAT. Several hydrogen bonding interactions occur between the water ring and the NAT surface, which provide extra-stabilization for alpha-NAT.

Metastable NAT could be one of the missing links to fully understand high altitude cloud formation. However, to date,



alpha-NAT had not been investigated to the same degree as stable beta-NAT. We first solved the structure of alpha-NAT, which enabled the calculation of the vibrational spectra. Inconsistencies between experiment and calculation lead us to the conclusion that all alpha-NAT samples always contain small ice domains or clusters, which are responsible for the spectral differences. Quantum calculations on water adsorption of selected surfaces of both crystals point to the same conclusion. In our former publications we found an interaction between ice and alpha-NAT which prolongs the lifetime of metastable NAT even at elevated temperatures [14]. A possible explanation is the presence of a hexagonal arrangement of water in the alpha-NAT structure, which favors interaction with ice.

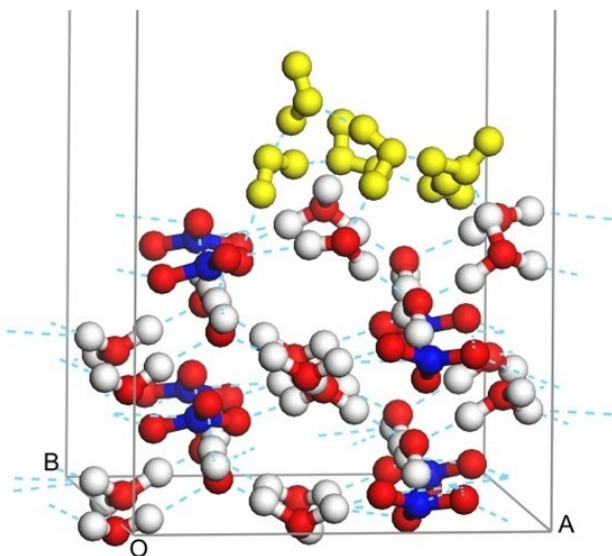


**Figure 4:** Close-up view of the structure of a water-ring on {001} surface of alpha-NAT. This structure yields the largest (in absolute number) adsorption energy for a six-membered-ring of water (in yellow) on {001} surface of alpha-NAT.

Our structural point of view is strongly supported by experiments on alpha-NAT growth followed by monitoring FTIR absorption upon depositing  $\text{HNO}_3$  on a thin water ice film (see supplementary information section for further details). We emphasize the absence of a nucleation barrier at characteristic UT/LS (<188 K) temperatures in the presence of water ice. In addition, the conversion of alpha-NAT to stable beta-NAT takes place spontaneously under the present experimental conditions (187.5 – 195 K). We therefore clearly distinguish three phases of NAT growth: (i) formation of alpha-NAT, (ii) spontaneous conversion of alpha- to beta-NAT in a narrow temperature window of observation (187.5 – 195 K), and (iii) subsequent growth of beta-NAT up to 195.5 K. In contrast to Zondlo et al. but in agreement with earlier work cited in [20] we do not observe the formation of an amorphous liquid  $\text{HNO}_3/\text{H}_2\text{O}$  layer upon admission of  $\text{HNO}_3$  to a pure thin ice film. Therefore we may modify the PSC Ia formation process by introducing two simplifications: (a) initial formation of an amorphous  $\text{HNO}_3/\text{H}_2\text{O}$  liquid is not necessary as metastable alpha-NAT is spontaneously generated in a heterogeneous nucleation process, on an ice substrate, without a nucleation barrier; and (b) crystallization processes are occurring directly as a result of gas-phase deposition without necessitating slow crystallization processes from the liquid. Hence, alpha-NAT can either form a matrix embedding crystalline ice particles or in turn being embedded itself inside a matrix of ice.

We conclude that, in the atmosphere, the formation of NAT proceeds at  $T < 188$  K (frost point in UT/LS) through the metastable alpha-NAT phase, which subsequently rearranges to the stable beta-NAT with increasing temperature. At  $T > 195$  K alpha-NAT is not observable due to fast conversion kinetics and only beta-NAT is seen. It seems clear that the barrierless growth of alpha-NAT provides strong evidence for the high affinity of NAT towards water ice which will have to be taken into account in growth scenarios for PSC's in the LS and cirrus clouds in the UT.

## Experimental Section

Ostwald's step rule states that in general it is not the most stable but the least stable polymorph that crystallises first [22]. This is a tendency in nature observed for the polymorphism of many molecular solids. Starting from a disordered sample (amorphous or supercooled) the less ordered crystalline phase is formed, which in general is the metastable modification. Following this idea, we have produced amorphous NAT on a gold-plated support by quenching small droplets (2  $\mu\text{m}$ ) generated by a nebulizer (Meinhard TR-50-A1). Using this technique, we were able to produce amorphous nitric acid/water samples of various concentrations. Annealing and crystallization gave access to three new metastable hydrate phases [23–24] one of which is alpha-NAT at a concentration of 25 mol% (53.8 wt%). The sample amount, however, was always insufficient for high quality diffraction experiments which would make the crystalline structure accessible. We have solved this problem now by spraying directly into liquid nitrogen (77 K). In this procedure the nebulizer was situated about 30 mm above the liquid surface allowing rapid heat exchange. Samples produced on the gram scale have been investigated by X-ray diffraction, neutron diffraction and inelastic neutron scattering experiments. After production the sample was kept at 77 K or below and the amorphism was confirmed in the corresponding experiments. Subsequently, the sample was annealed above the glass transition point (155 K) starting crystallization of the low-temperature polymorph. Since the phase transition is irreversible, data collection was started at the lowest temperature possible in the cryostat system. Afterwards, the sample was annealed above the alpha/beta phase transition temperature (180 K). Again, measurements were carried out at lowest temperature due to the irreversibility of the phase change.

The structure of alpha-NAT was computationally converged using periodic density functional theory with the plane wave pseudopotential method as implemented in the CASTEP code [25], with gradient-corrected functional and PBE parametrization [29] employing a plane wave cut-off of 830 eV. This computational method, GGA-PBE, is usually employed in the simulation of molecular solids similar to our system [30, 31, 32]. Strict convergence criteria were selected for geometry optimization and vibrational spectrum calculation ( $5 \times 10^{-6}$  eV/atom, 0.01 eV/Å, 0.0001 Å and 0.02 GPa for energy, maximum force, maximum displacement and maximum stress, respectively). The experimental structure was relaxed in the geometry optimization process keeping the cell parameters fixed to the measured values. The INS spectra were recorded using the broadband (0 – 4000  $\text{cm}^{-1}$ ), high resolution spectrometer TOSCA [24] at the ISIS Facility. For the calculated INS spectrum of alpha-NAT, we used again the CASTEP code [25] with the parameterization described before. Phonon frequencies were obtained by diagonalisation of the dynamical matrix computed using density-functional perturbation theory [26]. The atomic displacements in each mode that are part of the CASTEP output, enable visualization of the modes to aid assignments and are also all that is required to generate the INS spectrum using the program ACLIMAX [27].

FTIR spectra are recorded by co-adding 10 scans at a resolution of 4  $\text{cm}^{-1}$  with a Bruker 113v spectrometer for the measurements done at TU Vienna, respectively with a Biorad FTS-575C for measurements done at PSI. For details regarding the setup of each spectrometer see [23] (TU) or [19] (PSI), respectively.

Neutron diffraction experiments were carried out at the high-resolution powder diffractometer SPODI [28] at the neutron source Heinz Maier-Leibnitz (FRM II) in Garching near Munich, Germany. The data were collected in the scattering angular range of 0–160° with 0.05° stepwidth and a wavelength of 1.5482 Å using a germanium (551) monochromator.

The X-ray diffraction experiments were conducted at the XRC (Vienna University of Technology) using an Xpert Pro Powder Diffractometer (PANalytical) attached with a cryo-stage (Oxford Ltd.). An Xcelerator detector with an active scanning length of 2.122° was used and measurements were carried out at CuK $\alpha$  wavelength using a nickel filter.

## Acknowledgements

This research project has been supported (in part) by the European Commission under the 7th Framework Program through the Key Action: Strengthening the European Research Area, Research Infrastructures. We acknowledge neutron beam time at ISIS and at the FRM II. The X-ray measurements were carried out within the X-ray Center of the Vienna University of Technology. HG and FW are grateful for financial support by the Austria Science Funds (FWF) project P23027. OG acknowledges financial support from Ministerio de Ciencia e Innovación, "Ramón y Cajal" program, Projects FIS2010-16455 and CGL2013-48415. RI and MJR would like to acknowledge the generous funding of the Swiss National Science Foundation under projects no. 200020\_125204 and 200020\_144443/1.

Received: ((will be filled in by the editorial staff))

Published online on ((will be filled in by the editorial staff))

**Keywords:** Ice Clouds • Diffraction • Vibrational Spectroscopy • Atmospheric Chemistry • PSCs

- [1] S. Solomon, R.R. Garcia, F.S. Rowland, D.J. Wuebbles, *Nature* **1986**, 321, 755–758.
- [2] C. Voigt, J. Schreiner, A. Kohlmann, P. Zink, K. Mauersberger, N. Larsen, T. Deshler, C. Kröger, J. Rosen, A. Adriani, F. Cairo, G. Donfrancesco, M. Viterbini, J. Ovarlez, H. Ovarlez, C. David, A. Dörnbrack, *Science* **2000**, 290, 1756–1758.
- [3] J. Schreiner, C. Voigt, C. Weisser, A. Kohlmann, K. Mauersberger, T. Deshler, C. Kröger, J. Rosen, N. Kjome, N. Larsen, A. Adriani, F. Cairo, G. Di Donfrancesco, J. Ovarlez, H. Ovarlez and A. Dörnbrack, *J. Geophys. Res.* **2003**, 108, D58313.
- [4] M. Hopfner, N. Larsen, R. Spang, B. P. Luo, J. Ma, S. H. Svendsen, S. D. Eckermann, B. Knudsen, P. Massoli, F. Cairo, G. Stiller, T. V. Clarmann, and H. Fischer, *Atmos. Chem. Phys.* **2006**, 6, 1221–1230.
- [5] T. Koop, U.M. Biermann, W. Raber, B.P. Luo, P.J. Crutzen, T. Peter, *Geophys. Res. Lett.* **1995**, 22, 917–920.
- [6] D.A. Knopf, T. Koop, B.P. Luo, U.G. Weers, T. Peter, *Atmos. Chem. Phys.* **2002**, 2, 207–214.
- [7] C. Voigt, H. Schlager, B. P. Luo, A. Dörnbrack, A. Roiger, P. Stock, J. Curtius, H. Vossing, S. Borrmann, S. Davies, P. Konopka, C. Schiller, G. Shur, and T. Peter, *Atmos. Chem. Phys.* **2005**, 5, 1371–1380.
- [8] C. R. Hoyle, I. Engel, B. P. Luo, M. C. Pitts, L. R. Poole, J.-U. Groöb, and T. Peter, *Atmos. Chem. Phys.* **2013**, 13, 9577–9595.
- [9] O. Stetzer, *Atmos. Chem. Phys.* **2006**, 6, 3023–3033.
- [10] P.J. Popp, R.S. Gao, T.P. Marcy, D.W. Fahey, P.K. Hudson, T.L. Thompson, B. Kaercher, B.A. Ridley, A.J. Weinheimer, D. Knapp, D.D. Montzka, D. Baumgardner, T. Garrett, E. Weinstock, J. Smith, D. Sayres, J. Pittman, S. Dhaniyala, T. Bui, and M. Mahoney, *J. Geophys. Res.-Atmos.* **2004**, 109, D06302.
- [11] R.S. Gao, P.J. Popp, D.W. Fahey, T.P. Marcy, R.L. Herman, E.M. Weinstock, D. Baumgardner, T.J. Garrett, K.H. Rosenlof, T.L. Thompson, T.P. Bui, B.A. Ridley, S.C. Wofsy, O.B. Toon, M.A. Tolbert, B. Karcher, T. Peter, P.K. Hudson, A.J. Weinheimer, and A.J. Heymsfield, *Science* **2004**, 303, 516–520.
- [12] T.L. Malkin, B.J. Murray, A.V. Brukhno, J. Anwar, O.G. Salzmann, *Proc. Natl. Acad. Sci. USA* **2012**, 109, 1041–1045.
- [13] W.F. Kuhs, C. Sippel, A. Falenty, T.C. Hansen, *Proc. Natl. Acad. Sci. USA* **2012**, 109 (52), 21259–21264.
- [14] H. Grothe, H. Tizek, D. Waller, and D. Stokes, *Phys. Chem. Chem. Phys.* **2006**, 8, 2232–2239.
- [15] alpha-NAT: ICSD-No.: 426542. beta-NAT: ICSD-No.: 1902.
- [16] TOPAS: Version 4.2, Bruker AXS GmbH, Karlsruhe, 2009.
- [17] J.C. Li, *J. Chem. Phys.* **1996**, 105, 6733–6755.
- [18] B.M. Llorente, **2010** PhD. Thesis. UAM-CSIC.
- [19] R. Iannarelli and M.J. Rossi, *J. Geophys. Res. Atmos.*, **2015**, 120.
- [20] M.A. Zondlo, P.K. Hudson, A.J. Prenni, M.A. Tolbert, *Ann. Rev. Phys. Chem.* **2000**, 51, 473–499.
- [21] H. Grothe, H. Tizek, D. Waller, D.J. Stokes, *Phys. Chem. Chem. Phys.* **2006**, 8, 2232–2239.
- [22] W. Ostwald, *Zeitschrift für Physikalische Chemie* **1897**, 22, 289–330.
- [23] H. Tizek, E. Knözinger, H. Grothe, *Phys. Chem. Chem. Phys.* **2004**, 6, 972–979.
- [24] D. Colognesi, M. Celli, F. Cilloco, R.J. Newport, S.F. Parker, V. Rossi-Albertini, F. Sacchetti, J. Tomkinson and M. Zoppi, *Appl. Phys. A [Suppl.]* **2002**, 74, S64–S66.
- [25] S. J. Clark, M. D. Segall, C. J. Pickard, P. J. Hasnip, M. J. Probert, K. Refson, and M. C. Payne, *Z. Krist.* **2005**, 220, 567–570.
- [26] V. Milman, A. Perlov, K. Refson, S. J. Clark, J. Gavartin, and B. Winkler, *J. Phys.: Condens. Matter* **2009**, 21, 485404.
- [27] A.J. Ramirez-Cuesta, *Comput. Phys. Commun.* **2004**, 157, 226.
- [28] M. Hoelzel, A. Senyshyn, N. Juenke, H. Boysen, W. Schmahl, H. Fuess, *Nucl. Inst. Meth. Phys. Res.* **2012** A667: 32.
- [29] Perdew, J.P.; Burke, K.; Ernzerhof, M., *Phys. Rev. Lett.*, **1996**, 77, 3865–3868.
- [30] B. M. Giuliano, R. M. Escibano, R. Martín-Doménech, E. Dartois, G. M. Muñoz Caro, *A&A*, **2004** 565, A108.
- [31] W. Xiaoxin, M. Fengxian, M. Chunli, C. Hang, L. Zhenxian, Z. Hongyang, W. Xiaol and C. Qiliang, *JCP*, **2014**, 141, 024703.
- [32] M. Dračinský, M. Šalab and P. Hodgkinson, *CrystEngComm*, **2014**, 16, 6756.

Entry for the Table of Contents (Please choose one layout)

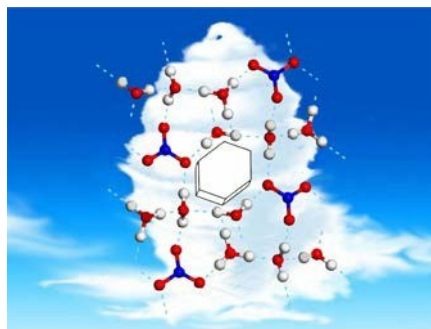
Layout 1:

***The unknown phase***

Fabian Weiss, Frank Kubel, Oscar Galvez, Markus Hoelzel, Stewart F. Parker, P. Baloh, Riccardo Iannarelli, Michel J. Rossi and Hinrich Grothe\*

\_\_\_\_\_ **Page – Page**

Metastable Nitric Acid Trihydrate in Ice Clouds



A new-found structure sheds light on the early stages of ice cloud formation in the stratosphere/upper troposphere.

## Details of QM calculations on the alpha- and beta-NAT structures

The structure of alpha-NAT was computationally converged using periodic density functional theory with the plane wave pseudopotential method as implemented in the CASTEP code [25], with gradient-corrected functional and PBE parametrization employing [29, 32] a plane wave cut-off of 830 eV. As was mentioned in the main paper, this method is usually employed in similar molecular solid systems [30, 31, 32]. Strict convergence criteria were selected for geometry optimization and vibrational spectrum calculation ( $5 \times 10^{-6}$  eV/atom, 0.01 eV/Å, 0.0001 Å and 0.02 GPa for energy, maximum force, maximum displacement and maximum stress, respectively). The calculated and experimental geometrical parameters of the structures in the unit cell of alpha- and beta-NAT are collected in Table S1. Nice agreement is obtained between experimental and calculated bond distances including the intermolecular hydrogen bond. In order to evaluate the importance of dispersion interactions, geometry optimization and infrared spectra was also calculated including DFT-D method with the Grimme parametrization [S1]. Only minor modifications in the structure (see Table S1) and infrared spectra, both alpha and beta phases, are obtained when the DFT-D method is included (see Fig. S1), so, due to the increase of the computation time this correction was not incorporated in the calculations.

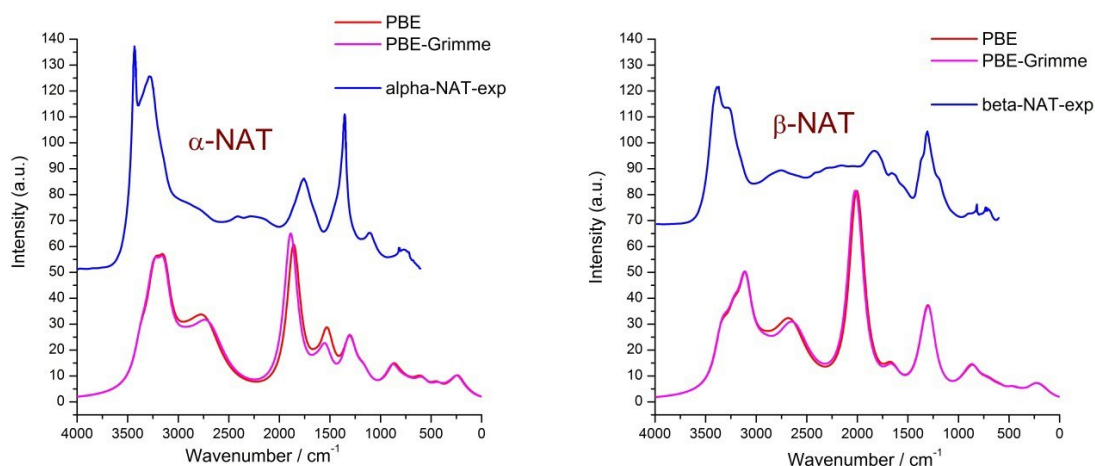


Figure S1.

A comparison between alpha- and beta-NAT spectra is shown in Fig. S2. Although our calculated IR spectra encompass intrinsic limitations due to the theoretical method used (harmonic approximation and no information on the width of the bands), band positions are reasonably well predicted. Even, the red-shift of the “scissor mode” of hydronium (bands around 1900 to 1700  $\text{cm}^{-1}$ ) for the alpha-NAT in comparison of the beta-phase, is qualitatively well predicted by the calculated spectra. However, the highest frequency peak in the alpha phase (at approx. 3500  $\text{cm}^{-1}$ ) could not be reproduced by our predicted spectra. Different methods have been tested (PBE, PBE+Grimme, PW91, SIESTA, [S2]), and in all the cases, the high frequency region of alpha- and beta-phase spectra show similar vibrational modes that could not explain the strong, sharp peak at 3500  $\text{cm}^{-1}$  found for the experimental alpha-NAT spectrum. For these reasons, we conclude that it should be due to dangling OH bonds of pure crystalline ice inclusions.

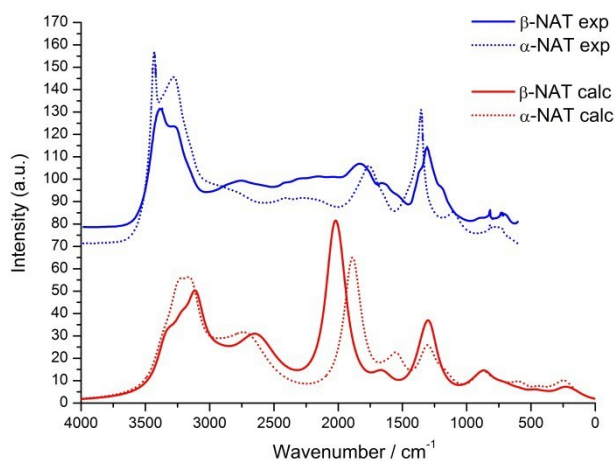


Figure S2.



Table S1. Geometrical parameters of the structures of alpha- and beta-NAT

Parameter	PBE	PBE <sub>Grimme</sub>	Exp.	PBE	PBE <sub>Grimme</sub>	Exp.
	$\alpha$ -NAT			$\beta$ -NAT		
r(N-O)	1.263	1.264	1.247	1.266	1.267	1.273
r(N-O)	1.282	1.282	1.285	1.261	1.262	1.272
r(N-O)	1.265	1.266	1.216	1.282	1.283	1.290
r(H-O) <sub>H3O+</sub>	1.101	1.096	1.079	1.026	1.029	1.034
r(H-O) <sub>H3O+</sub>	1.020	1.023	1.029	1.086	1.085	1.110
r(H-O) <sub>H3O+</sub>	1.011	1.011	1.009	1.013	1.012	1.015
r(H-O) <sub>H2O</sub>	0.983	0.984	0.997	0.996	0.996	1.007
r(H-O) <sub>H2O</sub>	0.996	0.996	0.986	0.987	0.987	0.997
r(H-O) <sub>H2O</sub>	0.992	0.993	1.047	0.996	0.996	1.007
r(H-O) <sub>H2O</sub>	0.991	0.991	0.972	0.987	0.987	1.001
r(H $\cdots$ O) <sub>NO3<math>\cdots</math>H2O</sub>	1.764	1.780	1.764	1.806	1.816	1.788
r(H $\cdots$ O) <sub>NO3<math>\cdots</math>H2O</sub>	1.721	1.729	1.769	1.713	1.717	1.713
r(H $\cdots$ O) <sub>NO3<math>\cdots</math>H2O</sub>	1.805	1.809	1.857	1.784	1.776	1.750
r(H $\cdots$ O) <sub>NO3<math>\cdots</math>H3O+</sub>	1.634	1.645	1.627	1.614	1.632	1.653
r(H $\cdots$ O) <sub>H3O+<math>\cdots</math>H2O</sub>	1.356	1.370	1.385	1.376	1.387	1.361
r(H $\cdots$ O) <sub>H3O+<math>\cdots</math>H2O</sub>	1.588	1.578	1.549	1.546	1.539	1.556
r(H $\cdots$ O) <sub>H2O<math>\cdots</math>H2O</sub>	1.772	1.768	1.853	1.738	1.730	1.692

For the evaluation of the interaction of water molecules on alpha- and beta-NAT surfaces, we have selected the {001} surfaces composed of two slabs and a pseudo vacuum of  $\sim 20$  Å for both crystals (see Figure S3 for a graphical representation of both surfaces). The choice of the {001} face was based on previous studies that showed that this face is the energetically most favorable for adsorption of HCl in beta-NAT crystals [S3]. In addition, previous theoretical studies on beta-NAT surfaces have shown that two slabs of comparable thickness is computationally optimal for these type of calculations [S4].

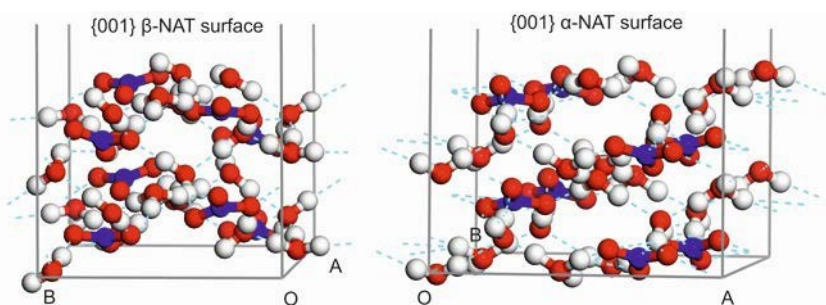


Figure S3.

After relaxation of both surfaces, employing less strict criteria than for the optimization of the unit cell ( $2 \times 10^{-5}$  eV/atom, 0.05 eV/Å, 0.002 Å and 0.1 GPa for energy, maximum force, maximum displacement and maximum stress, respectively), due to the increase of the computational effort, a water molecule was deposited on the top of the surface. Eight and six different adsorption sites were tested for beta- and alpha-NAT surfaces, respectively. The tested sites were based both on preliminary MM calculations (by the Adsorption Locator module of the Material Studio package [S5]) and a certain degree of chemical intuition. The adsorption energies (in absolute values) range from 4.8 to 13.7 and 7.3 to 20.3 kcal.mol<sup>-1</sup>, for beta-NAT and alpha-NAT respectively. According to these results, the {001} alpha-NAT surface shows a markedly stronger interaction with a water molecule compared to beta-NAT. Fig. S4 shows the structures of the strongest water adsorption sites for both surfaces.

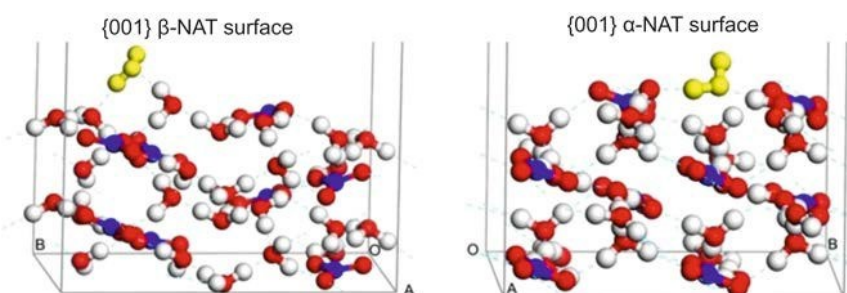


Figure S4.

To explore the interaction further, we included more molecules in the water adsorption process. A set of six water molecules, in a six-membering configuration similar to  $I_h$ , was deposited on both surfaces. A couple of configurations were tested for both surfaces. The largest calculated adsorption energy is 18.4 and 37.5 kcal mol<sup>-1</sup>, for beta-NAT and alpha-NAT respectively. Again, the latter surface shows a noticeably larger affinity for water adsorption. Fig.S5 shows the most favorable geometry for a six-molecule-ring adsorbed on the {001} alpha-NAT surface.



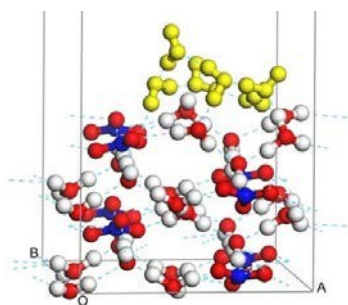


Figure S5.

#### Experimental Apparatus and Growth Protocol: Stirred Flow Reactor Studies

Deposition and evaporation experiments were conducted in a multidagnostic Stirred Flow Reactor (SFR) whose design and operation have been described before [S6-S7]. The special feature of the experiment is the design of the cryostat holding a temperature-controlled optical Si window adapted for FTIR transmission experiments of thin ice films deposited in the range 170 – 180 K. The cryostat is thermally insulated such that the only cold spot with which the gas within the SFR interacts is the optical window. In this way the interaction of the gas with the cold surface (deposition, evaporation, chemical transformation) can be monitored quantitatively either using residual gas mass spectrometry or FTIR absorption spectroscopy for changes in gas- and condensed phase composition, respectively. Wall adsorption to the stainless steel vessel walls of the SFR for H<sub>2</sub>O and HNO<sub>3</sub> are taken into account by measured Langmuir adsorption isotherms at 315 K. During the build-up of alpha-NAT on a pure water ice film the partial pressure of HNO<sub>3</sub> was in the range  $5 \cdot 10^{-8}$  to  $8 \cdot 10^{-7}$  mbar in agreement with the equilibrium vapor pressure of NAT according to published phase diagrams and commensurate with the HNO<sub>3</sub> background pressure in the UT/LS at 60 mbar total pressure and 10 ppb HNO<sub>3</sub> mixing ratio. The alpha-NAT phase was constructed starting typically with deposition of HNO<sub>3</sub> on a 1  $\mu$ m thick ice film distributed equally on two sides of a silicon window in the range 180 to 185 K. The sample is exposed to a HNO<sub>3</sub> flow in the range  $3\text{--}7 \times 10^{14}$  molecule s<sup>-1</sup> and showed self-limiting behaviour at a dose of  $2\text{--}3 \times 10^{17}$  HNO<sub>3</sub> compared to  $4 \times 10^{18}$  H<sub>2</sub>O in the ice film. The rate of diffusion of HNO<sub>3</sub> across a film of alpha-NAT significantly slowed compared to the formation of the new phase which fact is displayed in the left panel of Fig. S6 (red trace). For the conversion of alpha- to beta-NAT that is observable in the range 187.5-195 K the reactor is set to static conditions during the phase transformation in order to prevent loss of HNO<sub>3</sub>. Subsequently, experiments on beta-NAT are continued under SFR conditions. In addition, the numerous isosbestic points (8) displayed in the temporal sequence of the composite FTIR absorption spectra (Fig. S6, right panel) underline the fact that the formation of alpha-NAT is a simple elementary step of the type  $3\text{H}_2\text{O} + \text{HNO}_3 \rightarrow \text{alpha-HNO}_3 \cdot 3\text{H}_2\text{O}$  without the involvement of a stable intermediate on the time scale of a FTIR measurement (45 to 90 sec). The stoichiometry of alpha-NAT has been verified using mass balance arguments for H<sub>2</sub>O and HNO<sub>3</sub> using both calibrated mass spectrometric signals as well as optical densities in the IR spectral range [S7]. The conversion from alpha- to the thermodynamically stable beta-NAT is observable under static conditions of the SFR without loss of HNO<sub>3</sub> upon pumping in the range 187.5 to 195 K also under conditions where several isosbestic points (4) appear (not shown). This again points towards a 1:1 conversion alpha-NAT  $\rightarrow$  beta-NAT observed in the range 187.5-195 K without mechanistic complications such as the presence of an intermediate. Figure S7 displays the deconvoluted mid-IR spectra of pure alpha- and beta-NAT in the absence of excess (pure) ice whose principal peak positions and comparison with published composite NAT + ice spectra have been given in Tables S2a and S2b.

Table S2a: Principal peak positions in wavenumbers (cm<sup>-1</sup>) of the alpha-NAT IR absorption spectrum.

Type of vibration	Tolbert and Middlebrook [S8]	Ritzhaupt and Devlin [S9]	Koehler et al. [S10]	This work
$\nu_3$ (H <sub>2</sub> O)	3427	3424	3430	3430
$\nu_1$ (H <sub>2</sub> O)	3230	3203	3210	3233
$\nu_4$ (H <sub>3</sub> O <sup>+</sup> )	1765	1753	1760	1760
$\nu_3$ (NO <sub>3</sub> <sup>-</sup> )	1384	1393	1380	1385

Table S2b: Principal peak positions in wavenumbers (cm<sup>-1</sup>) of the beta-NAT IR absorption spectrum.

Type of vibration	Koehler et al. [S10]	This work
$\nu_3$ (H <sub>2</sub> O)	3375	3370
$\nu_1$ (H <sub>2</sub> O)	3220	3233
$\nu_4$ (H <sub>3</sub> O <sup>+</sup> )	1850	1846
$\nu_3$ (NO <sub>3</sub> <sup>-</sup> )	1375	1377
$\nu_3$ (NO <sub>3</sub> <sup>-</sup> )	1340	1339

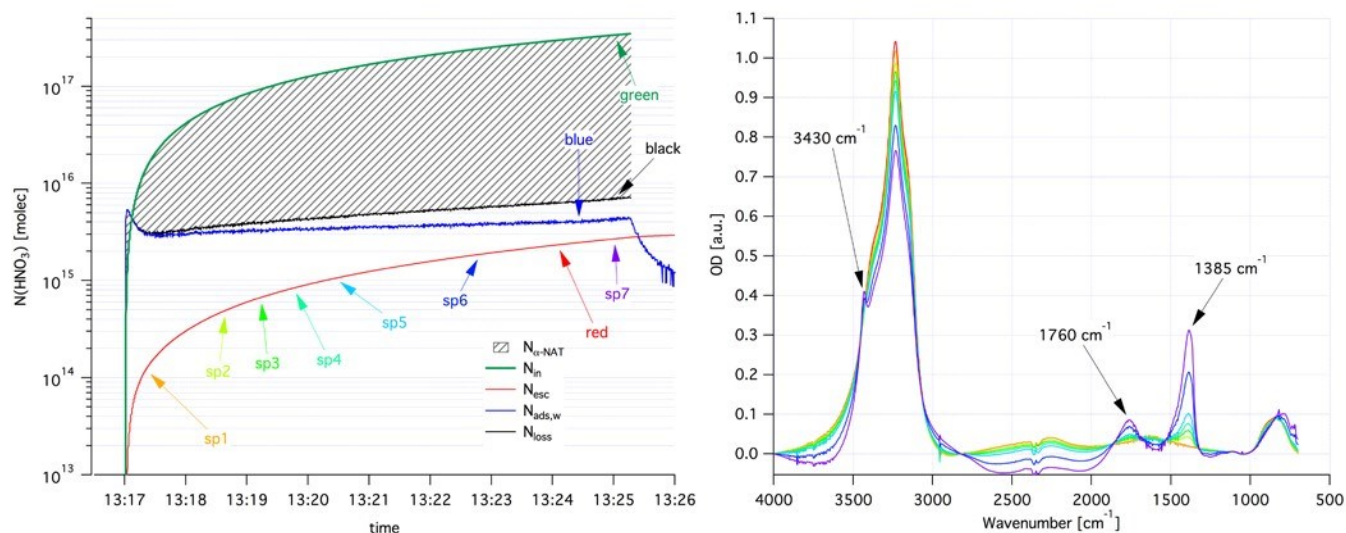


Figure S6.

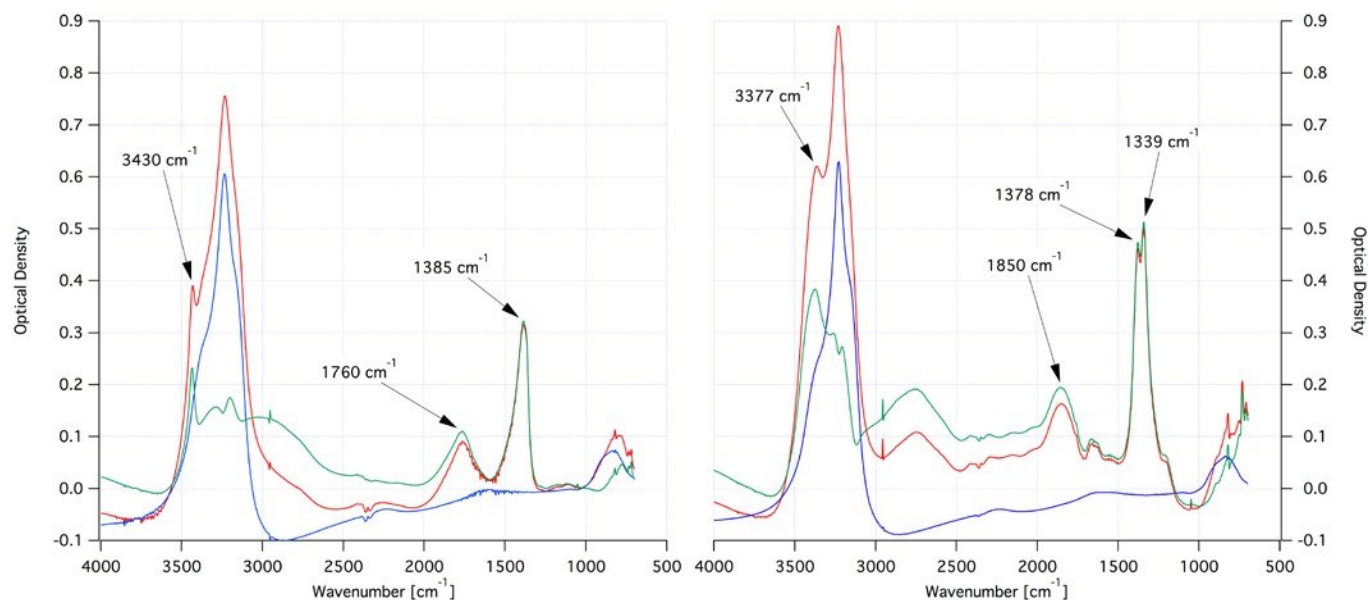


Figure S7.

## References

- S1. S. Grimme, *J. Comput. Chem.*, **2006**, 27, 1787
- S2. J. M. Soler, *J. Phys.: Condens. Matter*, **2002**, 14, 2745
- S3. Y.A. Mantz, F.M. Geiger, L.T. Molina, M.J. Molina, B.L.A. Trout *J. Phys. Chem* **2002**, A 106, 6972.
- S4. B.M. Llorente *PhD. Thesis* **2010** UAM-CSIC.
- S5. Accelrys Software Inc., Materials Studio Release Notes, Release 7.0, San Diego: Accelrys Software Inc. **2013**.
- S6. R. Iannarelli, M.J. Rossi *Atmos. Chem. Phys.* **2014**, 14, 5183-5204.
- S7. R. Iannarelli and M.J. Rossi, *J. Geophys. Res. Atmos.*, **2015**, 120.
- S8. M.A. Tolbert, A.M. Middlebrook *J. Geophys. Res.* **1990**, 95, 22423-22431.
- S9. G. Ritzhaupt, J.P. Devlin *J. Phys. Chem.* **1991**, 95, 90-95.
- S10. B.G. Koehler, A.M. Middlebrook, M.A. Tolbert *J. Geophys. Res.* **1992**, 97, 8065-8074.

## Figure Legends

Figure S1. Experimental and theoretical infrared spectra of alpha- and beta-NAT.

Figure S2. Comparison between experimental and theoretical infrared spectra of alpha- and beta-NAT.

Figure S3: Graphical representation of {001} surface of beta- (left panel) and alpha-NAT (right panel).

Figure S4: View of the structures with largest (in absolute number) energy values for the adsorption of a water molecule (in yellow) on {001} surface of beta- (left panel) and alpha-NAT (right panel).

Figure S5: View of the structure with largest (in absolute number) adsorption energy value for a six-member-ring of water molecules (in yellow) on the {001} surface of alpha-NAT.

Figure S6: HNO<sub>3</sub> deposition onto pure ice film at 182 K. The right panel shows the temporal evolution of the composite FTIR absorption spectrum starting with pure ice (red trace) and ending with a mixture of alpha-NAT and ice (purple trace). The left panel shows cumulative numbers of molecules: blue: HNO<sub>3</sub> admitted into SFR (N<sub>in</sub>), red: HNO<sub>3</sub> lost through effusion out of SFR (N<sub>esc</sub>), green: HNO<sub>3</sub> lost to the stainless steel walls of SFR (N<sub>ads,w</sub>), black: total loss of HNO<sub>3</sub> (sum of red and blue, N<sub>loss</sub>). The total HNO<sub>3</sub> adsorbed on ice corresponds to the grey area between the green and the black trace (N<sub>alpha-NAT</sub>). The color-coded labels correspond to the FTIR spectra in the right panel.

Figure S7: FTIR absorption spectrum of alpha- (left) and beta-NAT (right) at 183 and 195 K, respectively. The spectrum of the H<sub>2</sub>O/ice NAT mixture (red) is deconvoluted into the pure H<sub>2</sub>O ice (blue) and alpha- and beta-NAT (green) spectra, respectively. Characteristic absorptions are labeled in the corresponding spectra.

## Structure Solution

For the structure solution of the unknown and unindexed compound, the program package TOPAS [1a] was calibrated with an Y<sub>2</sub>O<sub>3</sub> pattern provided as a standard pattern. As sensitive parameter, the sample tilt factor was found and set as a fixed parameter to the unknown pattern of the new phase. Impurity analysis showed the presence of ice modification I<sub>n</sub> which was strongly textured. Indexing by TOPAS of the unknown reflection set based on the 25 first intensities gave a monoclinic structure. The following hkl fit procedure [2a] allowed to determine as highest possible space group P 1 2<sub>1</sub>/a 1. Lattice parameters of a~12.97, b~10.97, c~3.35 Å and beta~87.3° were found. By calculation of the unit cell volume (476.5 Å<sup>3</sup>) it was possible to estimate the number of molecular units in the unit cell. Already known systems were used as reference. Best estimation was one NO<sub>3</sub> unit and three D<sub>2</sub>O units and one individual D<sup>-</sup> ion. Structure solution using FOX [3a] with rigid units converged to a reasonable model with expected interatomic distances. After a first constrained fit using TOPAS, the atomic positions were unconstrained and refined to a stable structure model. (leaving vibrational values constrained). After optimization of very few supplementary refinement parameters (e.g. insignificant local texture (100): 0.96, crystal size: 72(2) nm, local strain parameter: 0.54(1) and 6 background factors, zero error: 0.003(1), all together 71 parameters were refined. After completion of the refinement, a R<sub>Bragg</sub> = 1.5% was obtained. Lattice parameters and refinement data are given in Table 1, atomic positions in Table 2. Interatomic distances are given in Table 3.

[1a] TOPAS: Version 4.2, Bruker AXS GmbH, Karlsruhe, Germany, 2009.

[2a] A. Le Bail, *Powder Diffraction* **2005**, 20, 316-326.

[3a] V. Favre-Nicolin, R. Cerny, *J. Appl. Crystallogr.* **2002**, 35, 734-743.

Table 1a

Formula	D14 N2 O12
Molar mass / g mol <sup>-1</sup>	248.16
Crystal system	monoclinic
Space group	P121/a1
Temperature / K	159
a / Å	12.9721(6)
b / Å	10.9702(5)
c / Å	3.35250(16)
beta/ °	87.254(4)
unit cell volume / Å <sup>3</sup>	476.53(4)
cell formula units Z	2
density/ g cm <sup>-3</sup>	1.730
radiation wavelength / Å	1.5482 (neutron)
2 theta min / °	5
2 theta max / °	87
number of reflections	890
hkl	0..15; -12..13; -4..4
number of variables	56 positions and vibrational parameters, 4 lattice parameters

number of variables	15 pattern describing variables
R <sub>F</sub> /%	2.7
R <sub>w</sub> /%	3.8
R <sub>w</sub> expected /%	0.8
R <sub>Bragg</sub> /%	1.5
ICSD No.	426542

Table 2a

Atom	x	y	z	Uiso
N	.9083(2)	.2884(4)	.2528(12) .	0083(9)
O1	.9489(4)	.3845(6)	.3461(17) .	0049(4)
O2	.9592(4)	.1882(5)	.2736(17) .	0049(4)
O3	.8219(3)	.2842(6)	.1066(16) .	0049(4)
O11	.6441(4)	.2748(7)	.6262(16) .	0049(4)
D11	.5808(4)	.2875(7)	.4814(16) .	0184(5)
D21	.6985(4)	.2890(7)	.4149(16) .	0184(5)
O22	.1537(5)	.9960(7)	1.0383(19)	.0049(4)
D12	.1459(5)	1.0744(6)	.8694(17) .	0184(5)
D22	.1139(4)	.9325(6)	.9150(17) .	0184(5)
O33	.3368(5)	.9391(6)	.0633(18) .	0049(4)
D13	.2576(6)	.9653(6)	.0644(18) .	0184(5)
D23	.3464(5)	.8566(6)	.202(2) .	0184(5)
D33	.1210(5)	.5019(7)	.7970(19) .	0184(5)

Table 3a

N O1	1.227(8)
N O3	1.245(6)
N O2	1.286(7)
O1 D33	1.627(9)
O2 D22	1.763(9)
O2 D11	1.775(8)
O3 D21	1.863(7)
O11 D11	0.983(8)
O11 D21	0.988(7)
O11 D23	1.559(9)
O11 D12	1.844(9)
D11 D21	1.533(7)
O22 D22	0.971(9)
O22 D12	1.038(9)
O22 D13	1.395(10)
D12 D22	1.617(9)
D22 D13	1.985(9)
O33 D33	1.009(10)
O33 D23	1.029(9)
O33 D13	1.067(10)
D13 D33	1.712(10)
D13 D23	1.736(10)
D23 D33	1.650(10)